INTERNATIONAL JOURNAL FOR NUMERICAL METHODS IN ENGINEERING
Int. J. Numer. Meth. Engng 2005; **62**:122–157
Published online in Wiley InterScience (www.interscience.wiley.com). DOI: 10.1002/nme.1195

On hypersingular surface integrals in the symmetric Galerkin boundary element method: application to heat conduction in exponentially graded materials

Alok Sutradhar[1], Glaucio H. Paulino[1,*,†] and L. J. Gray[2]

[1]*Newmark Laboratory, Department of Civil and Environmental Engineering, University of Illinois at Urbana-Champaign, Newmark Laboratory, 205 North Mathews Avenue, Urbana, IL 61801, U.S.A.*
[2]*Oak Ridge National Laboratory, Computer Science and Mathematics Division, Oak Ridge National Laboratory, Bldg 6012, Oak Ridge, TN 37831, U.S.A.*

SUMMARY

A symmetric Galerkin formulation and implementation for heat conduction in a three-dimensional functionally graded material is presented. The Green's function of the graded problem, in which the thermal conductivity varies exponentially in one co-ordinate, is used to develop a boundary-only formulation without any domain discretization. The main task is the evaluation of hypersingular and singular integrals, which is carried out using a direct 'limit to the boundary' approach. However, due to complexity of the Green's function for graded materials, the usual direct limit procedures have to be modified, incorporating Taylor expansions to obtain expressions that can be integrated analytically. Several test examples are provided to verify the numerical implementation. The results of test calculations are in good agreement with exact solutions and corresponding finite element method simulations. Copyright © 2004 John Wiley & Sons, Ltd.

KEY WORDS: symmetric Galerkin; boundary element method; functionally graded materials; diffusion; hypersingular integrals; Green's function

1. INTRODUCTION

The symmetric Galerkin boundary element method (SGBEM) has emerged as a powerful numerical method in computational mechanics in recent years. The formulation possesses the attractive feature of producing a symmetric coefficient matrix [1–3] and, in addition, the Galerkin

*Correspondence to: G. H. Paulino, Newmark Laboratory, Department of Civil and Environmental Engineering, University of Illinois at Urbana-Champaign, 205 North Mathews Avenue, Urbana, IL 61801, U.S.A.
†E-mail: paulino@uiuc.edu

Contract/grant sponsor: University of Illinois at Urbana-Champaign
Contract/grant sponsor: National Science Foundation; contract/grant number: CMS-0115954
Contract/grant sponsor: U.S. Department of Energy; contract/grant number: DE-AC05-00OR22725

Received 31 March 2003
Revised 10 November 2003
Accepted 21 July 2004

approximation allows standard continuous C^0 elements to be used for evaluation of hypersingular integrals. These properties make the SGBEM suitable for coupling with the popular finite element method (FEM) [4]. The Galerkin technique has the important property of 'local support' that is especially suitable for treating corners, including the Dirichlet corners [5].

Although the development of the SGBEM started in the last decade, most of the computational implementations have concentrated in two-dimensional (2D) problems [6–9], however, recently a number of three-dimensional (3D) implementations have also been reported [10–13], mostly limited to homogeneous media. A review of various applications of the SGBEM can be found in the paper by Bonnet *et al.* [4], among others. The present paper emphasizes non-homogeneous media as described below.

Functionally graded materials or FGMs are those in which the composition and the volume fraction of constituents vary gradually, giving a non-uniform microstructure with continuously graded macroproperties (e.g. specific heat, conductivity, density). For instance, one face of a structural component (plate or cylinder) may be an engineering ceramic that can resist severe thermal loading, and the other face may be a metal to maintain structural strength and toughness. A comprehensive treatment of the science and technology of FGMs can be found in the book by Miyamoto *et al.* [14], and in the review article by Paulino *et al.* [15]. *The present work is concerned with the SGBEM formulation for heat transfer in FGMs*. The Galerkin (non-symmetric) formulation for FGMs using the singular boundary integral equation has been examined by Gray *et al.* [16] for steady-state problems, and by Sutradhar *et al.* [17, 18] for transient problems. A dual reciprocity boundary element method applied to heat conduction for FGMs has been reported by Tanaka *et al.* [19]. Chen [20, 21] has developed a collocation-based BEM for Darcy's flow with spatial variation of permeability and has presented closed-form Green's functions for various permeability functions.

One of the challenges in a 3D-SGBEM formulation is the evaluation of singular double surface integrals (four-dimensional integrals in parametric space). In a Galerkin approximation, the integration is carried out with respect to both the field point and the source point. For a numerical implementation, this means that the integrals are evaluated for every pair of elements. Singular integrals occur as the Green's function and its derivatives diverge when the field point approaches the source point. An integral is therefore singular if the elements are *coincident*, or are *adjacent*, sharing either an edge or a vertex. The required double integrations of hypersingular kernel functions have in a way limited the implementations of the SGBEM. In a broad sense, the strategies proposed to address such class of problems can be classified as regularization, finite part, and direct approach. The regularization techniques employ many procedures such as use of simple solutions, and application of Stokes theorem [10, 22, 23]. The finite part approach is based on extracting the principal value of the singular integral, and direct evaluation based on multiple analytic integration [24–27]. A direct approach [28, 29], using neither Stokes theorem nor finite-part integral, is revisited and adopted herein. As previous papers [28, 29] only considered the simple Laplace equation, *one of the goals of this work is to demonstrate that the direct 'limit to the boundary' approach works very well for evaluating the singular and hypersingular integrals for the special FGM Green's function. This approach is also helpful to treat other complicated Green's functions*.

In this paper, a SGBEM for heat conduction for FGMs is formulated. The implementation is a pure boundary-only formulation without any domain integral. It relies on the Green's function (GF) for the partial differential equation incorporating the material gradation. A direct treatment of the hypersingular double integrals using a hybrid analytical/numerical approach

is presented. In order to handle the complexity of the FGM Green's function, the direct limit approach of Reference [29] needs to be modified. This direct limit approach is shown to be suitable for dealing with complicated Green's functions, which appear in applications such as those involving FGMs.

The remaining sections of this paper are organized as follows. First, the Green's function and the governing equation for the FGM problem are presented. Second, the symmetric Galerkin formulation is shown. Next, the evaluation of hypersingular integrals is described. Afterwards, examples are provided that verify the formulation. Finally, the paper concludes with a few remarks followed by a brief discussion on directions for future research.

2. ON THE FGM GREEN'S FUNCTION

Steady-state isotropic heat conduction in a solid is governed by the equation

$$\nabla \cdot (k(x, y, z)\nabla\phi) = 0 \tag{1}$$

where $\cdot$ denotes the inner product, $\phi = \phi(x, y, z)$ is the temperature function, $k(x, y, z)$ is the thermal conductivity which can be a function of the Cartesian co-ordinates. Let the FGM be defined by the thermal conductivity that varies exponentially in one Cartesian co-ordinate, i.e.

$$k(x, y, z) = k(z) = k_0 \mathrm{e}^{2\beta z} \tag{2}$$

where β denotes the material non-homogeneity parameter. Substituting this material expression into Equation (1), one obtains

$$\nabla^2\phi + 2\beta\phi_z = 0 \tag{3}$$

where ϕ_z is the derivative of ϕ with respect to z, i.e.

$$\phi_z \equiv \partial\phi/\partial z \tag{4}$$

The Green's function is the solution to the adjoint equation with a delta function force, namely

$$\nabla^2 G(P, Q) - 2\beta G_z(P, Q) = -\delta(Q - P) \tag{5}$$

where δ denotes the Dirac delta function, P and Q denote the source point and the field point, respectively (Figure 1) and G_z is the derivative of G with respect to z. The solution of this equation is derived [16, 30] as

$$G(P, Q) = \frac{\mathrm{e}^{\beta(-r+R_z)}}{4\pi r} \tag{6}$$

where

$$R_z = z_Q - z_P, \quad P = (x_P, y_P, z_P), \quad Q = (x_Q, y_Q, z_Q) \quad \text{and} \quad r = \|\mathbf{R}\| = \|\mathbf{Q} - \mathbf{P}\| \tag{7}$$

The Green's function for the non-homogeneous problem is essential for developing a boundary-only integral equation formulation. Note that the Green's function for an FGM can be rewritten as [31]

$$G(P, Q) = \frac{1}{4\pi r} + \frac{\mathrm{e}^{\beta(-r+R_z)} - 1}{4\pi r} \tag{8}$$

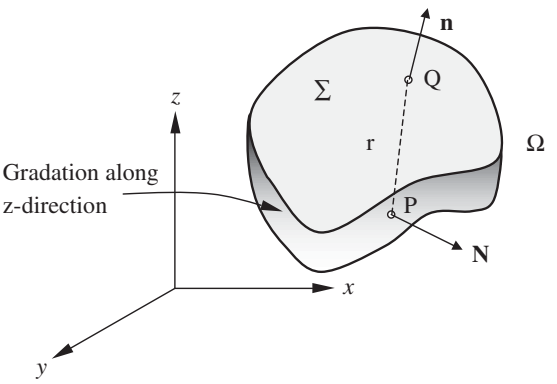

Figure 1. Illustration of a generic body with boundary Σ and domain Ω. The present SGBEM relies on a boundary-only formulation for FGMs. The source point is P (normal $\mathbf{N}$) and the field point is Q (normal $\mathbf{n}$).

The first term of Equation (8) is the Green's function for the Laplace equation in homogeneous media. The second term is bounded in the limit as $r \to 0$ and is a consequence of the grading; when β tends to zero (material is homogeneous), this graded term vanishes. This form shows that the singularity for the FGM Green's function is precisely the same as for the homogeneous. It will therefore not be surprising that the divergent terms in the hypersingular integral are the same as for the Laplace equation [29].

3. SYMMETRIC GALERKIN FORMULATION

The governing boundary integral equation corresponding to Equation (3) is

$$\phi(P) + \int_\Sigma \phi(Q) \left(\frac{\partial}{\partial n} G(P, Q) - 2\beta n_z G(P, Q) \right) \mathrm{d}Q = \int_\Sigma G(P, Q) \frac{\partial}{\partial n} \phi(Q) \, \mathrm{d}Q \tag{9}$$

which differs in form from the usual integral statements by the presence of the additional term multiplying $\phi(Q)$, i.e. $[-2\beta n_z G(P, Q)]$, due to the material gradation.

In the SGBEM, the symmetry comes from the symmetry properties of the kernel functions [4, 32]. For the homogeneous Laplace equation, the fundamental solution is symmetric, but the FGM Green's function, Equation (6), is not. In order to get symmetric kernels, the FGM boundary integral equations are re-formulated in terms of physical variables (flux instead of normal derivative), as described below. Thus, to obtain a symmetric matrix, the equations are written in terms of the surface flux,

$$\mathscr{F}(Q) = -k(z_Q) \frac{\partial}{\partial n} \phi(Q) \tag{10}$$

The boundary integral equation (BIE) for surface temperature $\phi(P)$ on the boundary Σ (see Figure 1) is therefore

$$\phi(P) + \int_\Sigma F(P, Q) \phi(Q) \, \mathrm{d}Q = \int_\Sigma G_S(P, Q) \mathscr{F}(Q) \, \mathrm{d}Q \tag{11}$$

and the kernel functions are

$$G_S(P,Q) = -\frac{G(P,Q)}{k(z_Q)} = -\frac{1}{4k_0\pi}\frac{\mathrm{e}^{\beta(-r-z_Q-z_P)}}{r}$$

$$F(P,Q) = \frac{\partial}{\partial n}G(P,Q) - 2\beta n_z G(P,Q) \tag{12}$$

$$= -\frac{\mathrm{e}^{\beta(-r+R_z)}}{4\pi}\left(\frac{\mathbf{n}\cdot\mathbf{R}}{r^3} + \beta\frac{\mathbf{n}\cdot\mathbf{R}}{r^2} + \beta\frac{n_z}{r}\right)$$

Notice that $G_S(P,Q)$, unlike $G(P,Q)$, is symmetric with respect to P and Q. This is one of the conditions needed for symmetry. The hypersingular boundary integral equation (HBIE) is obtained by differentiating Equation (11) with respect to the source P in the direction $\mathbf{N}$, which is normal to the boundary at P. In this case, however, it needs to be multiplied by $-k(z_P)$ to obtain the corresponding equation for surface flux, i.e.

$$\mathscr{F}(P) + \int_\Sigma W(P,Q)\phi(Q)\,\mathrm{d}Q = \int_\Sigma S(P,Q)\mathscr{F}(Q)\,\mathrm{d}Q \tag{13}$$

The kernel functions are computed as

$$S(P,Q) = -k(z_P)\frac{\partial}{\partial N}G_S(P,Q)$$

$$= \frac{\mathrm{e}^{\beta(-r-R_z)}}{4\pi}\left(\frac{\mathbf{N}\cdot\mathbf{R}}{r^3} + \beta\frac{\mathbf{N}\cdot\mathbf{R}}{r^2} - \beta\frac{N_z}{r}\right) \tag{14}$$

and

$$W(P,Q) = -k(z_P)\frac{\partial}{\partial N}F(P,Q)$$

$$= \frac{k_0}{4\pi}\mathrm{e}^{\beta(-r+z_Q+z_P)}\left(3\frac{(\mathbf{n}\cdot\mathbf{R})(\mathbf{N}\cdot\mathbf{R})}{r^5} + 3\beta\frac{(\mathbf{n}\cdot\mathbf{R})(\mathbf{N}\cdot\mathbf{R})}{r^4}\right.$$

$$+\frac{\beta^2(\mathbf{n}\cdot\mathbf{R})(\mathbf{N}\cdot\mathbf{R}) - \beta(N_z\mathbf{n} - n_z\mathbf{N})\cdot\mathbf{R} - \mathbf{n}\cdot\mathbf{N}}{r^3}$$

$$\left.-\beta\frac{\beta(N_z\mathbf{n} - n_z\mathbf{N})\cdot\mathbf{R} + \mathbf{n}\cdot\mathbf{N}}{r^2} - \beta^2\frac{N_z n_z}{r}\right) \tag{15}$$

The three symmetry requirements for the kernel functions are now fulfilled, i.e.

$$G_S(P,Q) = G_S(Q,P), \quad W(P,Q) = W(Q,P), \quad S(P,Q) = F(Q,P) \tag{16}$$

Interchanging Q and P implies replacing $\mathbf{N}(P)$ with $\mathbf{n}(Q)$ and changing the sign of $\mathbf{R}$, and thus all the conditions necessary for symmetry are seen to hold.

In this work, the direct limit procedure is employed to define and evaluate the singular integrals. If the limit is taken with the source point P approaching the boundary from *outside* the domain, then the 'free terms' $\phi(P)$ in the BIE (Equation (11)) and $\mathscr{F}(P)$ in the HBIE (Equation (13)) are not present. Thus, the exterior limit BIE and HBIE take the form

$$\begin{aligned} \mathscr{P}_s(P) &\equiv \int_\Sigma F(P, Q)\phi(Q)\,\mathrm{d}Q - \int_\Sigma G_S(P, Q)\mathscr{F}(Q)\,\mathrm{d}Q = 0 \\ \mathscr{F}_s(P) &\equiv \int_\Sigma W(P, Q)\phi(Q)\,\mathrm{d}Q - \int_\Sigma S(P, Q)\mathscr{F}(Q)\,\mathrm{d}Q = 0 \end{aligned} \tag{17}$$

where $\mathscr{P}_s$ denotes the equation for the surface temperature (potential) and $\mathscr{F}_s$ denotes the equation for the surface flux. The free terms are automatically incorporated in the '*exterior limit*' evaluation of the $F(P, Q)$ and $S(P, Q)$ integrals. Thus, a separate computation of these free terms is avoided, and they are obtained as a natural outcome of the direct limit procedure [33].

The surface temperature and surface flux are approximated in terms of values at element nodes Q_j and shape functions $\psi_j(Q)$, i.e.

$$\phi(Q) = \sum_j \phi(Q_j)\psi_j(Q), \quad \mathscr{F}(Q) = \sum_j \mathscr{F}(Q_j)\psi_j(Q) \tag{18}$$

In a Galerkin approximation, Equation (17) is enforced in an average sense, with the shape functions employed as the weighting functions. Therefore, the Galerkin boundary integral equations take the form

$$\int_\Sigma \psi_k(P)\mathscr{P}_s(P)\,\mathrm{d}P = 0 \tag{19}$$

$$\int_\Sigma \psi_k(P)\mathscr{F}_s(P)\,\mathrm{d}P = 0 \tag{20}$$

After discretization, the set of equations can be written in block-matrix form as $[H]\{\phi\} = [G]\{\mathscr{F}\}$, and in block-matrix these equations become

$$\begin{bmatrix} H_{11} & H_{12} \\ H_{21} & H_{22} \end{bmatrix} \begin{Bmatrix} \phi_{bv} \\ \phi_u \end{Bmatrix} = \begin{bmatrix} G_{11} & G_{12} \\ G_{21} & G_{22} \end{bmatrix} \begin{Bmatrix} \mathscr{F}_u \\ \mathscr{F}_{bv} \end{Bmatrix} \tag{21}$$

Symmetry of the coefficient matrix for a general mixed boundary value problem is achieved by the following simple arrangement. The BIE is employed on the Dirichlet surface, and the HBIE equation is used on the Neumann surface. The first row represents the BIE written on the Dirichlet surface, and the second row represents the HBIE written on the Neumann surface. Similarly, the first and the second columns arise from integrating over Dirichlet and Neumann surfaces, respectively. The subscripts in the matrix therefore denote known boundary values (bv) and unknown (u) quantities. Rearranging Equation (21) into the form $[\mathbf{A}]\{x\} = \{b\}$, one obtains

$$\begin{bmatrix} -G_{11} & H_{12} \\ G_{21} & -H_{22} \end{bmatrix} \begin{Bmatrix} \mathscr{F}_u \\ \phi_u \end{Bmatrix} = \begin{Bmatrix} -H_{11}\phi_{bv} + G_{12}\mathscr{F}_{bv} \\ H_{21}\phi_{bv} - G_{22}\mathscr{F}_{bv} \end{Bmatrix} \tag{22}$$

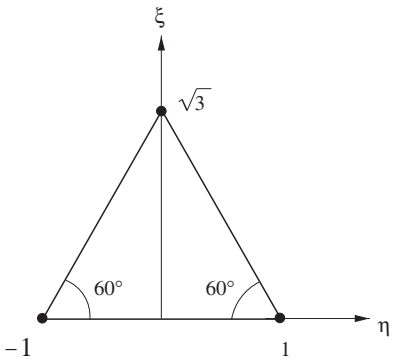

Figure 2. Isoparametric equilateral triangular linear element in $\{\eta, \xi\}$ space, where $-1 \leqslant \eta \leqslant 1,\ 0 \leqslant \xi \leqslant \sqrt{3}(1 - |\eta|)$.

The symmetry of the coefficient matrix, $G_{11} = G_{11}^{\mathrm{T}}$, $H_{22} = H_{22}^{\mathrm{T}}$, and $H_{12} = G_{21}$, now follows from the properties of the kernel functions (see Equation (16)).

In this paper, the analysis for a linear element will be considered in detail, as this forms the basis for handling higher-order interpolations. An equilateral triangle parameter space $\{\eta, \xi\}$, where

$$-1 \leqslant \eta \leqslant 1, \quad 0 \leqslant \xi \leqslant \sqrt{3}(1 - |\eta|) \tag{23}$$

will be employed (see Figure 2). This choice of parameter space is convenient for executing the coincident integration, as will be explained in the next section. The three linear shape functions are

$$\psi_1(\eta, \xi) = \frac{\sqrt{3}(1 - \eta) - \xi}{2\sqrt{3}}, \quad \psi_2(\eta, \xi) = \frac{\sqrt{3}(1 + \eta) - \xi}{2\sqrt{3}}, \quad \psi_3(\eta, \xi) = \frac{\xi}{\sqrt{3}} \tag{24}$$

4. EVALUATION OF SINGULAR DOUBLE INTEGRALS

For 3D problems, there are four typical configurations for the two elements containing source point P and field point Q (see Figure 3). Thus the following four distinct situations regarding the singularity must be considered:

- *Non-singular case*, when the source point P and the field point Q lie on distinct elements that do not share a common vertex or edge (Figure 3(a));
- *Coincident case*, when the source point P and the field point Q lie in the same element (Figure 3(b));
- *Edge-adjacent case*, when the source point P and the field point Q lie within adjacent elements that share a common edge (Figure 3(c)); and
- *Vertex-adjacent case*, when the source point P and the field point Q lie within adjacent elements that share only a common vertex (Figure 3(d)).

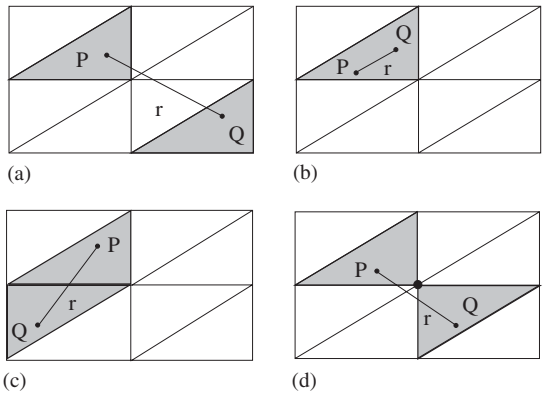

Figure 3. Four different cases considered for integration: (a) non-singular; (b) coincident; (c) edge adjacent; and (d) vertex adjacent.

The non-singular integrals can be evaluated using standard Gaussian quadrature formulas. In the direct limit approach for evaluating the singular integrals, the integrals for the coincident and the edge-adjacent cases are forced to be finite by moving the source P off the boundary in the direction $\mathbf{N}$ at a distance of ε. The next step is to employ polar co-ordinate transformations and then integrate analytically with a *fixed distance from the singularity*. After the exact integration, the limit $\varepsilon \to 0$ is considered. It will be demonstrated that the coincident and the edge-adjacent hypersingular integrals are separately divergent, producing terms of the form $\log(\varepsilon)$. However, the divergent terms from the coincident case can be shown to cancel out with the divergent terms from the edge-adjacent case, and therefore the divergent terms are removed exactly in this approach. Taking the limit $\varepsilon \to 0$ back to the boundary results in finite expressions, thus giving a well-behaved integral. Once the divergent terms have been identified and removed, the remaining terms of the integral can be evaluated using standard numerical quadrature. The discussion here about $\log(\varepsilon)$ singularity, etc. applies only to the hypersingular equation. The direct approach has been designed to handle this worst case, but apply equally to the less-singular integrals.

Compared to the simple Laplace equation treated in Reference [29], the challenge here is to work with the complicated hypersingular kernel function $W(P, Q)$, Equation (15). In particular, the exponential in this function precludes a complete analytic integration as in Reference [29], and thus additional procedures are required.

4.1. Coincident integration

The details of the procedure to evaluate the hypersingular integrals involving the kernel $W(P, Q)$ are described in this section. However, the integration of the kernels G_S, $S(P, Q)$ or $F(P, Q)$ can be handled in exactly the same manner, with the added simplification that no divergent terms appear in the limit $\varepsilon \to 0$. When the source point P and the field point Q lie within the same element E (see Figure 3(b)), $E_P = E_Q = E$, and the coincident integral to be evaluated is

$$\int_E \psi_k(P) \int_E \phi(Q) W(P, Q)\, \mathrm{d}Q\, \mathrm{d}P = \sum_{j=1}^{3} \phi(Q_j) \int_E \psi_k(P) \int_E \psi_j(Q) W(P, Q)\, \mathrm{d}Q\ \mathrm{d}P \tag{25}$$

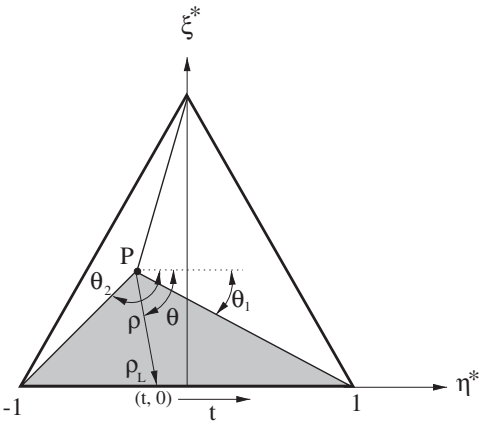

Figure 4. First polar co-ordinate transformation, $\{\eta^*, \xi^*\} \rightarrow \{\rho, \theta\}$, for the coincident integration. The variable t eventually replaces θ. Note that $P = P(\eta, \xi)$.

where E is defined by nodes P_k, $1 \leqslant k \leqslant 3$. Let the parametric variables for the outer P integration be denoted by (η, ξ), and that for Q by (η^*, ξ^*). Transfering the integral to the parametric space ($\mathrm{d}Q \rightarrow J_Q \mathrm{d}\xi^* \mathrm{d}\eta^*$ and $\mathrm{d}P \rightarrow J_P \mathrm{d}\xi \mathrm{d}\eta$) introduces the Jacobians J_Q and J_P. For coincident integration considering linear elements, the J_Q and J_P are equal and constant. The Jacobians can be conveniently incorporated into the hypersingular kernels, i.e.

$$J_P^2 W(P, Q) = \frac{k_0}{4\pi} \mathrm{e}^{\beta(-r+z_Q+z_P)} \left(3 \frac{(J_P \mathbf{N} \cdot \mathbf{R})^2}{r^5} + 3\beta \frac{(J_P \mathbf{N} \cdot \mathbf{R})^2}{r^4} + \frac{\beta^2 (J_P \mathbf{N} \cdot \mathbf{R})^2 - J_P^2}{r^3} - \beta \frac{J_P^2}{r^2} - \beta^2 \frac{(J_P N_z)^2}{r} \right) \tag{26}$$

First polar co-ordinate transformation $\{\eta^*, \xi^*\} \rightarrow \{\rho, \theta\}$: For the inner Q integration, the first step is to define a polar co-ordinate system centred at $P = (\eta, \xi)$,

$$\eta^* - \eta = \rho \cos(\theta), \quad \xi^* - \xi = \rho \sin(\theta) \tag{27}$$

as shown in Figure 4. Polar co-ordinate transformations centred at the singularity are particularly effective, as the Jacobian of the transformation, $\rho \, \mathrm{d}\rho$, reduces the order of the singularity. This aspect will be used in all the singular integrations.

The upper limit of ρ $(0 < \rho < \rho_L(\theta))$ is different for the three edges of the triangle and consequently, the (ρ, θ) integration is split into three sub-triangles (see Figure 4). It suffices to consider the calculation for the lower sub-triangle (shaded portion of the triangle in Figure 4). By exploiting the symmetry of the equilateral parametric space, the remaining sub-triangles are handled by rotating the element and employing the formulas for the lower sub-triangle associated with the edge $\xi^* = 0$.

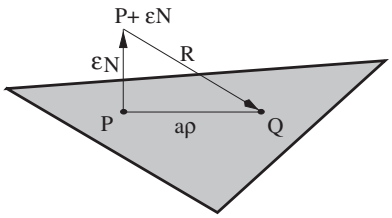

Figure 5. The source P is moved off the surface boundary in the direction of $\mathbf{N}$ at a distance of ε.

For the lower sub-triangle, the integration limits are

$$0 \leqslant \rho \leqslant \rho_L \quad \text{and} \quad \Theta_1 \leqslant \theta \leqslant \Theta_2 \tag{28}$$

where

$$\rho_L = -\frac{\xi}{\sin(\theta)}, \quad \Theta_1 = -\frac{\pi}{2} - \tan^{-1}\left(\frac{1+\eta}{\xi}\right), \quad \Theta_2 = -\frac{\pi}{2} + \tan^{-1}\left(\frac{1-\eta}{\xi}\right) \tag{29}$$

In the limit to the boundary approach as P is moved off the boundary in the direction of the source normal $\mathbf{N}$ at distance of ε, P is replaced by $P + \varepsilon\mathbf{N}$ for the exterior boundary limit (see Figure 5), therefore, the distance $r = \|\mathbf{Q} - \mathbf{P}\|$ takes the simple form

$$r^2(\rho, \theta) = \varepsilon^2 + a^2(\theta)\rho^2 \tag{30}$$

where

$$a^2(\theta) = a_{cc}\cos^2(\theta) + a_{cs}\cos(\theta)\sin(\theta) + a_{ss}\sin^2(\theta) \tag{31}$$

The three coefficients a_{cc}, a_{cs}, a_{ss}, depend solely upon the co-ordinates of the element nodes (a^2 is a positive quantity), i.e.

$$\begin{aligned} a_{cc} &= 1/4[(x_2 - x_1)^2 + (y_2 - y_1)^2 + (z_2 - z_1)^2] \\ a_{cs} &= 1/(2\sqrt{3})[(x_2 - x_1)(x_1 + x_2 - 2x_3) + (y_2 - y_1)(y_1 + y_2 - 2y_3) \\ &\quad + (z_2 - z_1)(z_1 + z_1 - 2z_3)] \\ a_{ss} &= 1/12[(y_1 + y_2 - 2y_3)^2 + (x_1 + x_2 - 2x_3)^2 + (z_1 + z_2 - 2z_3)^2] \end{aligned} \tag{32}$$

Here $P_k = (x_k, y_k, z_k)$, $(k = 1, 2, 3)$ are the (x, y, z) co-ordinates of the element nodes.

The term $J_P\mathbf{N} \cdot \mathbf{R}$ in the kernel (see expression (26)) becomes $-\varepsilon J_P$ as P is moved to $P + \varepsilon\mathbf{N}$. The shape function of P, $\psi_j(P)$ is a function of η and ξ. With the polar co-ordinate transformation centred on P (Equation (27)), the shape function $\psi_j(Q)$ is a linear function of ρ, i.e.

$$\psi_j(Q) = c_{j,0}(\eta, \xi) + c_{j,1}(\eta, \xi, \theta)\rho = \sum_{m=0}^{1} c_{j,m}\rho^m \tag{33}$$

$$\psi_j(P) = c_{j,0}(\eta, \xi) \tag{34}$$

As a result of the polar transformation, $(z_Q - z_P)$ can be written as $\alpha\rho$ where α is a function of θ and z co-ordinates of the element vertices, i.e.

$$\alpha = \frac{1}{2}\cos(\theta) + \frac{1}{2\sqrt{3}}(2z_3 - z_1 - z_2)\sin(\theta) \tag{35}$$

Since $e^{2\beta z_P}$ is independent of ρ, it is taken outside of the ρ integral, and the exponential term in Equation (26) can be written as

$$\begin{aligned} e^{\beta(-r+z_Q+z_P)} &= e^{\beta(-r+z_Q-z_P+2z_P)} \\ &= e^{2\beta z_P} e^{\beta\left(-\sqrt{\varepsilon^2+a^2\rho^2}+\alpha\rho\right)} \end{aligned} \tag{36}$$

Employing the boundary limit procedure and expressing the kernel function in polar co-ordinates, one obtains Equation (25) as

$$\begin{aligned} &\frac{1}{4\pi}\sum_{m=0}^{1}\int_{-1}^{1} d\eta \int_{0}^{\sqrt{3}(1-|\eta|)} \psi_k(\eta,\xi)\, d\xi \int_{\Theta_1}^{\Theta_2} c_{j,m}\, d\theta \int_{0}^{\rho_L} \rho^{m+1} \\ &\times e^{\beta\left(-\sqrt{\varepsilon^2+a^2\rho^2}+\alpha\rho\right)} \left(\frac{3\varepsilon^2 {J_P}^2}{(\varepsilon^2+a^2\rho^2)^{5/2}} - \frac{{J_P}^2}{(\varepsilon^2+a^2\rho^2)^{3/2}} + \frac{3\beta\varepsilon^2 {J_P}^2}{(\varepsilon^2+a^2\rho^2)^2} \right. \\ &\left. + \frac{\beta^2\varepsilon^2 {J_P}^2}{(\varepsilon^2+a^2\rho^2)^{3/2}} - \frac{\beta {J_P}^2}{\varepsilon^2+a^2\rho^2} - \frac{\beta^2 {J_P^z}^2}{\sqrt{\varepsilon^2+a^2\rho^2}} \right) d\rho \end{aligned} \tag{37}$$

Here J_P^z denotes $J_P N_z$, which is the Jacobian J_P multiplied by the z component of the normal at P, i.e. N_z.

First Taylor expansion of the exponential function: Due to the exponential term in the kernel, it is not possible to integrate the entire expression analytically. Our goal for analytic integration is to explicitly identify the divergent terms in the integral. This can be done by employing a Taylor expansion of the exponential term. Expanding up to the first two terms is sufficient to identify the divergent terms, i.e.

$$e^{\beta\left(-\sqrt{\varepsilon^2+a^2\rho^2}+\alpha\rho\right)} = 1 + \beta\left(-\sqrt{\varepsilon^2+a^2\rho^2}+\alpha\rho\right) + \mathcal{O}(\rho^2) \tag{38}$$

As the remainder of the expansion is of order ρ^2, this expansion leads to a sufficiently well behaved expression for the remainder of the integral so that numerical quadrature can be safely used.

First analytical integration (*on* ρ): Incorporating the Taylor expansion, the integral to be evaluated analytically is

$$\sum_{m=0}^{1}\int_0^{\rho_L}\rho^{m+1}\left(1+\beta\left(-\sqrt{\varepsilon^2+a^2\rho^2}+\alpha\rho\right)\right)\left(\frac{3\varepsilon^2 {J_P}^2}{(\varepsilon^2+a^2\rho^2)^{5/2}}\right.$$
$$\left.-\frac{{J_P}^2}{(\varepsilon^2+a^2\rho^2)^{3/2}}+\frac{3\beta\varepsilon^2{J_P}^2}{(\varepsilon^2+a^2\rho^2)^2}+\frac{\beta^2\varepsilon^2{J_P}^2}{(\varepsilon^2+a^2\rho^2)^{3/2}}-\frac{\beta{J_P}^2}{\varepsilon^2+a^2\rho^2}-\frac{\beta^2(J_P^z)^2}{\sqrt{\varepsilon^2+a^2\rho^2}}\right)\mathrm{d}\rho \quad (39)$$

For $m=0$ (see Equation (33)), the exact analytical integration results in

$$F_0=\frac{\beta^3}{2}(J_P^z)^2\left(1-\frac{\alpha}{a}\right)\rho_L^2+\frac{\beta^2}{a}\left[\left(1-\frac{\alpha}{a}\right){J_P}^2-(J_P^z)^2\right]\rho_L$$
$$+2\beta{J_P}^2\frac{\alpha}{a^3}+\beta{J_P}^2\frac{\alpha}{a^3}\log(\varepsilon)+\frac{{J_P}^2}{a^3\rho_L} \quad (40)$$

All terms are well behaved at $\varepsilon=0$ except for the last two. However the expression

$$\frac{\alpha\beta{J_P}^2\log(\varepsilon)}{a^3} \quad (41)$$

is *not* the divergent term that is being sought. It is easily seen that this term cancels out in the subsequent integration over θ. As the term does not contain ρ_L, a complete integration over $0\leqslant\theta\leqslant 2\pi$ can be considered. Note that α is a linear function of $\cos(\theta)$ and $\sin(\theta)$, and thus satisfies $\alpha(\pi+\theta)=-\alpha(\theta)$. From Equation (31), $a(\pi+\theta)=a(\theta)$, and from Equation (33), $c_{j,m}$ is independent of θ for $m=0$. Hence, the subsequent integration of the $\log(\varepsilon)$ term on expression (41) results in zero, i.e.

$$-\log(\varepsilon)c_{j,0}(\eta,\xi){J_P}^2\int_0^{2\pi}\frac{\alpha\beta}{a^3}\,\mathrm{d}\theta=0 \quad (42)$$

For $m=1$, the analytical integration becomes,

$$F_1=\frac{\beta^3}{2}(J_P^z)^2\left(1-\frac{\alpha}{a}\right)\rho_L^3+\frac{\beta^2}{2a}\left[\left(1-\frac{\alpha}{a}\right){J_P}^2-(J_P^z)^2\right]\rho_L^2$$
$$+2\frac{{J_P}^2}{a^3}+\frac{{J_P}^2}{a^3}\log\varepsilon-{J_P}^2\frac{\log(a\rho_L)}{a^3} \quad (43)$$

A divergent term similar to expression (41) also appears in this case. This term is also seen to cancel out in the subsequent integration over θ. The coefficient $c_{j,1}(\eta,\xi,\theta)$ is linear in $\cos(\theta)$ and $\sin(\theta)$, and therefore satisfies $c_{j,1}(\eta,\xi,\pi+\theta)=-c_{j,1}(\eta,\xi,\theta)$. Thus

$$-\log(\varepsilon){J_P}^2\int_0^{2\pi}\frac{c_{j,1}(\eta,\xi,\theta)}{a^3}\,\mathrm{d}\theta=0 \quad (44)$$

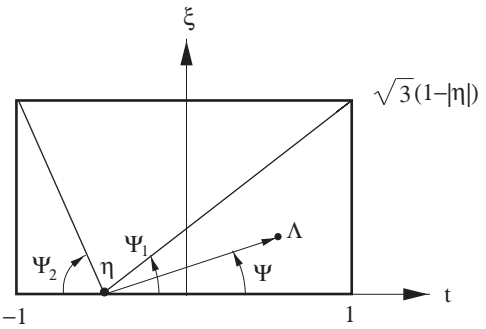

Figure 6. Geometry of the second polar co-ordinate transformation, $\{t, \xi\} \rightarrow \{\Lambda, \Psi\}$, for the coincident integration.

This first analytic integration is not sufficient to display the divergent term, and the subsequent integration on θ will not pose any problem. It is the next integration on ξ, (cf. Equation (37)) which has to be dealt with analytically. The analytic integration over ρ produces results that behave as $1/\rho_L$ (see the last term in Equation (40)) and, from Equation (29), $\rho_L = -\xi/\sin(\theta)$. This term is capable of producing a $\log(\varepsilon)$ contribution upon ξ integration with the lower limit of $\xi = 0$. Therefore, it is necessary to interchange the order of the integration on θ and ξ in order to identify the divergent term through analytical integration.

Variable tranformation $\{\theta\} \rightarrow \{t\}$: As the limits of the θ integration (i.e. Θ_1 and Θ_2) depend on ξ and η, the integration on the variable θ and ξ is not interchangeable.To circumvent this problem, a new variable t $(-1 \leqslant t \leqslant 1)$ is introduced via

$$\theta = -\frac{\pi}{2} + \tan^{-1}\left(\frac{t-\eta}{\xi}\right), \quad \frac{\mathrm{d}\theta}{\mathrm{d}t} = \frac{\xi}{\xi^2 + (t-\eta)^2} \tag{45}$$

which also results in $\rho_L = (\xi^2 + (t-\eta)^2)^{1/2}$. As depicted in Figure 4, t is the 'end-point' $(t, 0)$ of ρ on the ξ^*-axis.

Interchanging the order of integration and tranforming the variable from $\theta \rightarrow t$, the integral (cf. Equation (39)) for $m = 0$ can be written as

$$\frac{J_P^2}{4\pi} \int_{-1}^{1} \mathrm{d}\eta \int_{-1}^{1} \mathrm{d}t \int_{0}^{\sqrt{3}(1-|\eta|)} \psi_k(\eta, \xi)\, c_{j,0}\, F_0(\rho_L)\, \mathrm{d}\xi \tag{46}$$

Second polar co-ordinate transformation $\{t, \xi\} \rightarrow \{\Lambda, \Psi\}$: From Equation (45), the singularity is now at $t = \eta$, $\xi = 0$, and another polar co-ordinate transformation $\{\Lambda, \Psi\}$, replacing $\{t, \xi\}$, is employed (see Figure 6),

$$t = \Lambda\cos(\Psi) + \eta, \quad \xi = \Lambda\sin(\Psi) \tag{47}$$

The goal is to integrate Λ analytically. With the two changes of variables, $\theta \rightarrow t$ and $\{t, \xi\} \rightarrow \{\Lambda, \Psi\}$, $\cos(\theta)$ becomes $\cos(\Psi)$ and $\sin(\theta)$ becomes $-\sin(\Psi)$. Thus, $a(\theta)$, Equation (31), becomes simply $a(\Psi)$ and is a constant as far as the Λ integration is concerned. As shown in Figure 6, the $\{t, \xi\}$ domain is a rectangle, and integrating over $\{\Lambda, \Psi\}$ will necessitate a

decomposition into three subdomains

$$0 \leqslant \Psi \leqslant \Psi_1,\ \Psi_1 \leqslant \Psi \leqslant \pi - \Psi_2 \quad \text{and} \quad \pi - \Psi_2 \leqslant \Psi \leqslant \pi \tag{48}$$

where

$$\Psi_1 = \tan^{-1}\left(\frac{\sqrt{3}(1-|\eta|)}{1-\eta}\right), \quad \Psi_2 = \tan^{-1}\left(\frac{\sqrt{3}(1-|\eta|)}{1+\eta}\right) \tag{49}$$

Second Taylor expansion of the exponential function: With this final co-ordinate transformation, the P shape functions are linear in Λ, as are the coefficients $c_{j,m}$ from the Q shape functions. Part of the exponential term, $e^{2\beta z_P}$, which was previously kept outside of the ρ integral (cf. Equation (36)), is a linear function of Λ, and this term has to be included in the integration on Λ. In order to integrate analytically, a Taylor expansion of the exponential term is once again necessary. Note that z_P has a constant part which is independent of Λ,

$$z_P = z_P^0 + \Lambda z_P^1 \tag{50}$$

Thus the term $e^{2\beta z_P^0}$ can be kept out of the Λ integration. The rest can be expanded up to three terms in order to obtain the necessary divergent term,

$$e^{2\beta\Lambda z_P^1} = 1 + 2\beta\Lambda z_P^1 + 2\beta^2\Lambda^2(z_P^1)^2 + \mathcal{O}(\Lambda^3) \tag{51}$$

Theoretically, two terms in the above expansion are sufficient, however, an additional term was considered for convergence of numerical results. A discussion on additional terms in the Taylor expansion employed in HBIEs has been presented by Gray and Paulino [34].

Second analytical integration (*on* Λ): The product of the shape functions of P and Q produces terms of Λ up to order 2. The integrals (cf. Equation (46)) to be evaluated are therefore of the form

$$-\frac{{J_P}^2}{4\pi}\int_{-1}^{1} d\eta \int \sin(\Psi)\, d\Psi \int_0 \Lambda^s\, f(\Lambda)\, d\Lambda \tag{52}$$

for $s = 0, 1, 2$ where $f(\Lambda)$ is a function of Λ. The missing limits of the Λ and Ψ integrals depend upon the particular sub-triangle in Figure 6 being considered. The Λ integrations for $s = 1$ and 2 are straightforward. For $s = 0$, a finite contribution plus a divergent term of the form

$$L_{kj}^c = \log(\varepsilon)\,\frac{J_P^2}{4\pi}\int_{-1}^{1} \hat{\psi}_k^0 \hat{\psi}_j^0\, d\eta \int_0^{\pi} \frac{\sin(\Psi)}{a^3}\, d\Psi \tag{53}$$

is found. Here, $\hat{\psi}_l^0$ are the shape functions evaluated at $\Lambda = \rho = 0$, as

$$\hat{\psi}_1^0 = \frac{1-\eta}{2}, \quad \hat{\psi}_2^0 = \frac{1+\eta}{2}, \quad \hat{\psi}_3^0 = 0 \tag{54}$$

Note that as $a = a(\Psi)$ is independent of η, Equation (53) simplifies to

$$L_{kj}^c = \log(\varepsilon)\,\frac{J_P^2}{4\pi}\,\frac{1+\delta_{kj}}{3}\int_0^{\pi} \frac{\sin(\Psi)}{a^3}\, d\Psi \tag{55}$$

where δ_{kj} is the usual Kronecker delta function and $1 \leqslant k, j \leqslant 2$. For $m = 1$, following the same procedure as above does not produce any divergent terms.

The divergent term L^c_{kj} is precisely the same as that obtained from the hypersingular *homogeneous* Laplace equation [29]. This comes as no surprise because the new feature in the FGM kernels is the exponential term. In the Taylor expansion,

$$e^{\beta r} = 1 + (\beta r) + \frac{(\beta r)^2}{2} + \frac{(\beta r)^3}{6} + \cdots \tag{56}$$

the leading constant is the most singular, the subsequent terms actually help to kill off the singularity. Thus the divergence comes from the first term of the expansion, which is exactly the same term for the Laplace equation. The important consequence of this observation is that it will not be necessary to prove that Equation (55) cancels with the corresponding divergence from the adjacent edge integration (obtained below). The proof in Reference [29] suffices to demonstrate this point.

4.2. Edge adjacent integration

In this case an edge is shared between the two elements as shown in Figure 3(c). Orient the elements so that the shared edge is defined by $\xi = 0$ in E_P, and $\xi^* = 0$ for E_Q, and the singularity occurs when $\eta = -\eta^*$.

First polar co-ordinate transformation $\{\eta^*, \xi^*\} \to \{\rho, \theta\}$: The first step is to employ polar co-ordinates for the Q integration [29],

$$\eta^* = \rho\cos(\theta) - \eta, \quad \xi^* = \rho\sin(\theta) \tag{57}$$

As shown in Figure 7(a), the θ integration must be split into two pieces (for simplicity the integrands are omitted, but it will be useful to retain the Jacobians of the transformations)

$$\int_{-1}^{1} \mathrm{d}\eta \int_{0}^{\sqrt{3}(1-|\eta|)} \mathrm{d}\xi \left[\int_{0}^{\Theta_1(\eta)} \mathrm{d}\theta \int_{0}^{L_1(\theta)} \rho \,\mathrm{d}\rho + \int_{\Theta_1(\eta)}^{\pi} \mathrm{d}\theta \int_{0}^{L_2(\theta)} \rho \,\mathrm{d}\rho \right] \tag{58}$$

where

$$L_1(\theta) = \frac{\sqrt{3}(1+\eta)}{\sin(\theta) + \sqrt{3}\cos(\theta)}, \quad L_2(\theta) = \frac{\sqrt{3}(1-\eta)}{\sin(\theta) - \sqrt{3}\cos(\theta)} \tag{59}$$

The break-point in θ,

$$\theta_1(\eta) = \frac{\pi}{2} - \tan^{-1}\left(\frac{\eta}{\sqrt{3}}\right) \tag{60}$$

is only a function of η. The integrations can therefore be rearranged as follows:

$$\int_{-1}^{1} \mathrm{d}\eta \int_{0}^{\theta_1(\eta)} \mathrm{d}\theta \int_{0}^{\sqrt{3}(1-|\eta|)} \mathrm{d}\xi \int_{0}^{L_1(\theta)} \rho \,\mathrm{d}\rho + \int_{-1}^{1} \mathrm{d}\eta \int_{\theta_1(\eta)}^{\pi} \mathrm{d}\theta \int_{0}^{\sqrt{3}(1-|\eta|)} \mathrm{d}\xi \int_{0}^{L_2(\theta)} \rho \,\mathrm{d}\rho \tag{61}$$

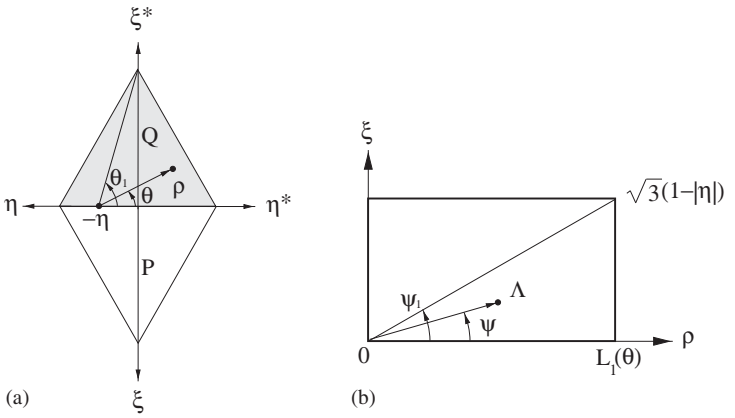

Figure 7. (a) Polar co-ordinate transformation employed in the Q element, $\{\eta^*, \xi^*\} \to \{\rho, \theta\}$; and (b) second polar co-ordinate transformation $\{\rho, \xi\} \to \{\Lambda, \Psi\}$ for the edge-adjacent integration.

Second polar co-ordinate transformation $\{\rho, \xi\} \to \{\Lambda, \Psi\}$: As the singularity occurs at $\rho = \xi = 0$, a second polar co-ordinate transformation is introduced

$$\rho = \Lambda \cos(\Psi), \quad \xi = \Lambda \sin(\Psi) \tag{62}$$

The Ψ integration must also be taken in two parts (Figure 7(b)), resulting in the four integrals

$$\int_{-1}^{1} \mathrm{d}\eta \int_{0}^{\Theta_1(\eta)} \mathrm{d}\theta \left[\int_{0}^{\Psi_1} \mathrm{d}\Psi \int_{0}^{\lambda_{11}} \cos(\Psi)\Lambda^2 \,\mathrm{d}\Lambda + \int_{\Psi_1}^{\pi/2} \mathrm{d}\Psi \int_{0}^{\lambda_{12}} \cos(\Psi)\Lambda^2 \,\mathrm{d}\Lambda \right]$$
$$+ \int_{-1}^{1} \mathrm{d}\eta \int_{\Theta_1(\eta)}^{\pi} \mathrm{d}\theta \left[\int_{0}^{\Psi_2} \mathrm{d}\Psi \int_{0}^{\lambda_{21}} \cos(\Psi)\Lambda^2 \,\mathrm{d}\Lambda + \int_{\Psi_2}^{\pi/2} \mathrm{d}\Psi \int_{0}^{\lambda_{22}} \cos(\Psi)\Lambda^2 \,\mathrm{d}\Lambda \right] \tag{63}$$

The formulas for the Λ limits are simply

$$\lambda_{n1} = L_n(\theta)/\cos(\Psi), \quad \lambda_{n2} = L_n(\theta)/\sin(\Psi) \tag{64}$$

for $n = 1, 2$. The distance function takes the form

$$r^2 = \varepsilon^2 + \varepsilon a_1 \Lambda + a_2 \Lambda^2 \tag{65}$$

but this quadratic expression (in the denominators) can be integrated exactly. The Λ^2 factor from the two polar transformations sufficiently reduces the order of the singularity such that one analytic integration (over Λ) will produce the $\log(\varepsilon)$ term.

Taylor expansion of the exponential function: The Λ integral cannot be evaluated analytically unless a Taylor expansion is once again utilized for the exponential term. To extract the divergent terms from this integral, a one term expansion will be enough (same arguments as for the coincident integration). Similarly to Equations (36) and (51), the exponential term for

this case can be written as

$$\begin{aligned} \mathrm{e}^{\beta(-r+z_Q+z_P)} &= \mathrm{e}^{\beta(-r+z_Q-z_P+2z_P)} \\ &= \mathrm{e}^{\beta\left(-\sqrt{\varepsilon^2+a^2\Lambda^2}+\alpha\Lambda+2(z_P^0+\Lambda z_P^1)\right)} \\ &= \mathrm{e}^{2\beta z_P^0}\mathrm{e}^{\beta\left(-\sqrt{\varepsilon^2+a^2\Lambda^2}+\alpha\Lambda+2\Lambda z_P^1\right)} \end{aligned} \tag{66}$$

The term $\mathrm{e}^{2\beta z_P^0}$ is taken outside of the Λ integration since it is independent of Λ. A one term Taylor expansion is employed in the remaining exponential term, i.e.

$$\mathrm{e}^{\beta\left(-\sqrt{\varepsilon^2+a^2\Lambda^2}+\alpha\Lambda+2\Lambda z_P^1\right)} = 1 + \mathcal{O}(\Lambda) \tag{67}$$

The rest of the expansion is of the order of Λ. This expansion along with the Λ^2 from the Jacobian of the polar transformation will be sufficient to provide a smooth function for numerical integration. This follows from the observation that $\Lambda = 0$ encapsulates all three conditions for $r = 0$, namely $\xi = \xi^* = 0$, and $\eta = -\eta^*$. Thus, as in the coincident algorithm, the exact integration is with respect '*to the distance from the singularity*'.

Analytical integration on Λ: The Λ integration results in a finite quantity plus a divergent contribution, which is given by

$$L_{kj}^e = \log(\varepsilon)\frac{1}{4\pi}\int_{-1}^{1}\hat{\psi}_k^0\,\hat{\psi}_j^0\,\mathrm{d}\eta\int_0^{\pi}\mathrm{d}\theta\int_0^{\pi/2}\cos(\Psi)\left(\frac{3J_{P\mathbf{N}}^1 J_{Q\mathbf{n}}^1}{a_2^{5/2}} - \frac{J_Q\mathbf{n}\bullet J_P\mathbf{N}}{a_2^{3/2}}\right)\mathrm{d}\Psi \tag{68}$$

where $J_{Q\mathbf{n}}^1$ and $J_{P\mathbf{N}}^1$ are the coefficients of Λ in $J_Q\mathbf{n}\bullet\mathbf{R}$ and $J_P\mathbf{N}\bullet\mathbf{R}$, respectively,

$$J_P\mathbf{N}\bullet\mathbf{R} = J_{P\mathbf{N}}^1\Lambda - J_P\varepsilon, \quad J_Q\mathbf{n}\bullet\mathbf{R} = J_{Q\mathbf{n}}^1\Lambda - J_Q\mathbf{n}\bullet\mathbf{N} \tag{69}$$

As in Equation (54), $\hat{\psi}_k^0$ and $\hat{\psi}_j^0$ denote the shape functions evaluated at $\Lambda = 0$. This expression, Equation (68), and the expression for L_{kj}^c, Equation (55), cancel one another. As noted above (Section 4.1), the proof of such cancellation is precisely the same as that for Laplace equation, which is given in Reference [29].

4.3. Vertex adjacent integration

In this case the singularity is limited to a single point in the four-dimensional integration (see Figure 3(d)). Orient the P and Q elements so that the singular point is $\eta = -1$ and $\eta^* = -1$.

Two polar co-ordinate transformations ($\{\eta^*, \xi^*\} \to \{\rho_q, \theta_q\}$, $\{\eta, \xi\} \to \{\rho_p, \theta_p\}$): Two separate polar co-ordinates are first introduced in each element (see Figure 8(a)),

$$\begin{aligned} \eta^* &= \rho_q\cos(\theta_q) - 1, \quad \xi^* = \rho_q\sin(\theta_q) \\ \eta &= \rho_p\cos(\theta_p) - 1, \quad \xi = \rho_p\sin(\theta_p) \end{aligned} \tag{70}$$

This results in an integral of the form

$$\int_0^{\pi/3}\mathrm{d}\theta_p\int_0^{L_p(\theta_p)}\rho_p\,\mathrm{d}\rho_p\int_0^{\pi/3}\mathrm{d}\theta_q\int_0^{L_q(\theta_q)}\rho_q\,\mathrm{d}\rho_q \tag{71}$$

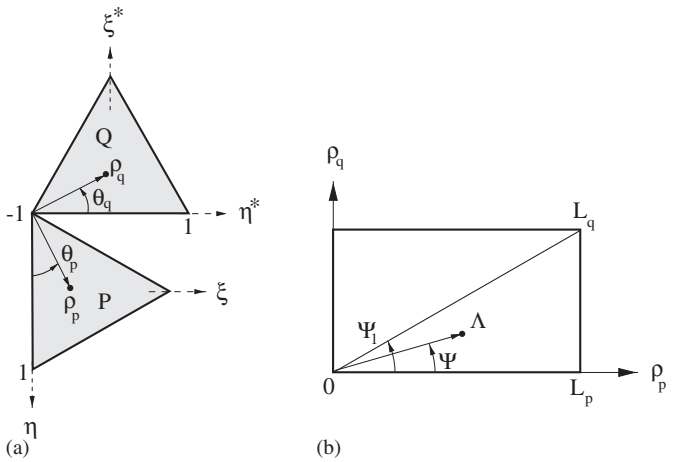

Figure 8. (a) Initial polar co-ordinate transformation employed in both P and Q elements; and (b) final polar co-ordinate transformation $\{\rho_p, \rho_q\} \rightarrow \{\Lambda, \Psi\}$ for the vertex adjacent integration.

where

$$L_p(\theta_p) = 2\sqrt{3}/\left[\sin(\theta_p) + \sqrt{3}\cos(\theta_p)\right], \quad L_q(\theta_q) = 2\sqrt{3}/\left[\sin(\theta_q) + \sqrt{3}\cos(\theta_q)\right] \tag{72}$$

As the vertex adjacent integration will not produce a divergent term, we omit the kernel function and just keep track of the Jacobians in the subsequent expressions. Now interchanging the order of the integration between ρ_p and θ_q, one obtains

$$\int_0^{\pi/3} \mathrm{d}\theta_p \int_0^{\pi/3} \mathrm{d}\theta_q \int_0^{L_p(\theta_p)} \rho_p \, \mathrm{d}\rho_p \int_0^{L_q(\theta_q)} \rho_q \, \mathrm{d}\rho_q$$

Third polar co-ordinate transformations $\{\rho_p, \rho_q\} \rightarrow \{\Lambda, \Psi\}$: The only singularity is at the common vertex $\rho_p = \rho_q = 0$, and thus a third polar co-ordinate transformation is performed

$$\rho_p = \Lambda\cos(\Psi), \quad \rho_q = \Lambda\sin(\Psi).$$

As illustrated in Figure 8(b), the $\{\rho_p, \rho_q\}$ domain is a rectangle, and thus the Ψ integration must be taken in two pieces. The combined Jacobian in this case is $\cos(\Psi)\sin(\Psi)\Lambda^3$, and thus Equation (71) becomes

$$\int_0^{\pi/3} \mathrm{d}\theta_p \int_0^{\pi/3} \mathrm{d}\theta_q \left[\int_0^{\Psi_1} \cos(\Psi)\sin(\Psi)\,\mathrm{d}\Psi \int_0^{L_1(\Psi)} \Lambda^3 \,\mathrm{d}\Lambda \right.$$
$$\left. + \int_{\Psi_1}^{\pi/2} \cos(\Psi)\sin(\Psi)\,\mathrm{d}\Psi \int_0^{L_2(\Psi)} \Lambda^3 \,\mathrm{d}\Lambda \right] \tag{73}$$

where

$$L_1(\Psi) = L_P(\theta_p)/\cos(\Psi) \quad \text{and} \quad L_2(\Psi) = L_Q(\theta_q)/\sin(\Psi) \tag{74}$$

With the Λ^3 factor multiplying the kernel function, it is possible to immediately set $\varepsilon = 0$, and the distance function is then $r^2 = a^2\Lambda^2$ (the coefficient being a function of all three angles and nodal co-ordinates). It is then immediately apparent that this integral is finite. Although numerical evaluation with Gaussian quadrature could be employed for the entire integration we prefer to execute the Λ integral semi-analytically in order to achieve better accuracy.

5. NUMERICAL IMPLEMENTATION

In this section, results for four test cases are reported, demonstrating the implementation of the above techniques. The evaluation of the singular integrals was carried out using the hybrid analytical/numerical integration integration explained in the previous section.

To verify the numerical implementation, the following FGM examples are presented:

(1) Cube with material gradation in z direction,
(2) Cube with material gradation in 45° with the z-axis,
(3) Sphere (interior Neumann),
(4) Compressor blade.

This set of examples comprise a severe test of the SGBEM code. The first example has analytical solution and is suitable for a mesh convergence study. The second example differs from the previous one by considering a different direction of material gradation, which is not aligned with any of the reference Cartesian axes. The third example consists of a Neumann problem and it is used to test the hypersingular BIE in the SGBEM implementation. Finally, the last example is a complicated engineering problem. All the above FGM problems can be verified for the homogeneous material case (constant conductivity) when the material non-homogeneity parameter vanishes ($\beta = 0$).

5.1. FGM cube with material gradation in z-direction

A simple FGM cube with constant temperature on two planes is considered first. As the analytical solution of this problem can be obtained, this problem is suitable for a convergence study. The problem of interest is shown in Figure 9. The top surface of the cube at $[z = 1]$ is maintained at a temperature of $T = 100$ while the temperature of the bottom face at $[z = 0]$ is zero. The remaining four faces are insulated (zero normal flux). The thermal conductivity is

$$k(x, y, z) = k_0 \mathrm{e}^{2\beta z} = 5\mathrm{e}^{2\beta z} \tag{75}$$

and various values of β will be considered. The analytical solution for the temperature is

$$\phi(x, y, z) = T\,\frac{1 - \mathrm{e}^{-2\beta z}}{1 - \mathrm{e}^{-2\beta L}} \tag{76}$$

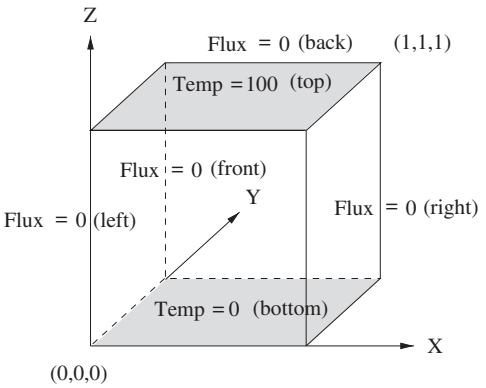

Figure 9. Geometry and boundary conditions of the FGM unit cube problem with constant temperature on two planes. The faces with prescribed temperature are shaded.

where L is the dimension of the cube (in the z-direction), and the analytical solution for the flux (on $z = 1$) is

$$q(x, y, z) = -k(x, y, z)\frac{2\beta T \mathrm{e}^{-2\beta z}}{1 - \mathrm{e}^{-2\beta L}} = -k_0 \frac{2\beta T}{1 - \mathrm{e}^{-2\beta L}} \tag{77}$$

The cube is discretized with 432 boundary elements and 294 nodes as shown in Figure 10(d). The computed temperature variation in the z direction is plotted with different values of β (material non-homogeneity parameter) and compared with the analytical solution in Figure 11. For this problem the flux on each face of the unit cube is constant. Figure 12 shows the variation of the flux on the face $z = 0$ with respect to the change of the material non-homogeneity parameter β, and compares the results with the analytical flux solution. For the face $z = 1$, the flux has the same variation as on the face $z = 0$, but with opposite sign (cf. Equation (77)).

The error in the temperature solution and the flux is computed considering various mesh discretizations (Figure 10) and employing a global error measure,

$$\mathscr{E} = \frac{1}{|u^{(\mathrm{e})}|_{\max}} \sqrt{\frac{1}{\mathrm{NP}} \sum_{I=1}^{\mathrm{NP}} \left[u_I^{(\mathrm{e})} - u_I^{(\mathrm{c})}\right]^2} \tag{78}$$

where $\mathscr{E}$ is the error in the solution, the superscripts (e) and (c) denote, respectively, the exact and the computed solutions, and NP is the total number of nodes. The four meshes illustrated in the Figure 10 were considered for this study. The computed global error with increasing number of elements is given in Table I, which shows that the global error reduces with mesh refinement (cf. Table I and Figure 10).

5.2. FGM cube with material gradation in 45° *with the z-axis*

The geometry and the boundary conditions for this example are the same as those in the previous example, except for the direction of the variation of the thermal conductivity. Here

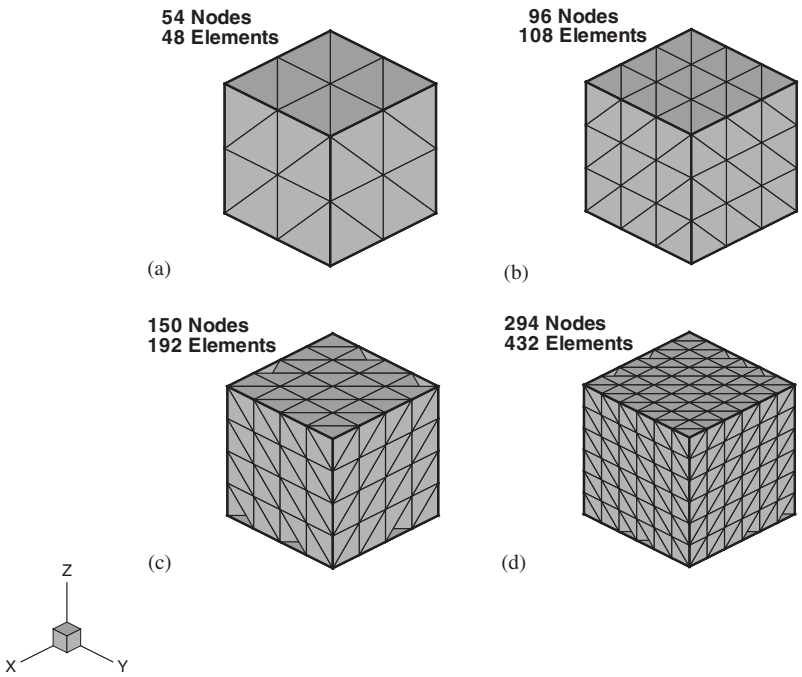

Figure 10. The four meshes used for the convergence study of the FGM cube problem.

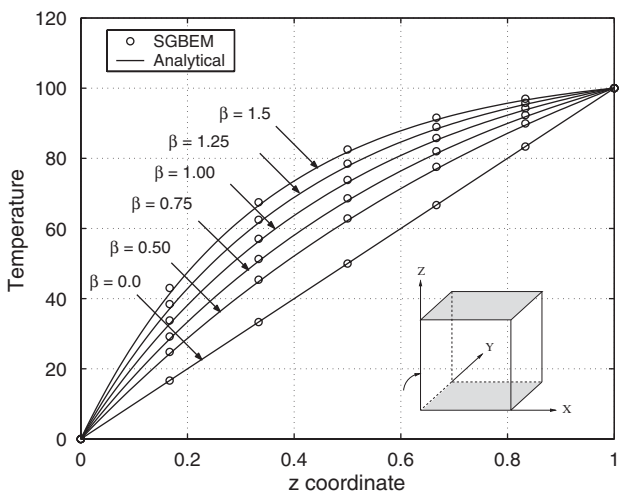

Figure 11. Temperature profile in z direction for the FGM cube discretized with 432 elements and 294 nodes.

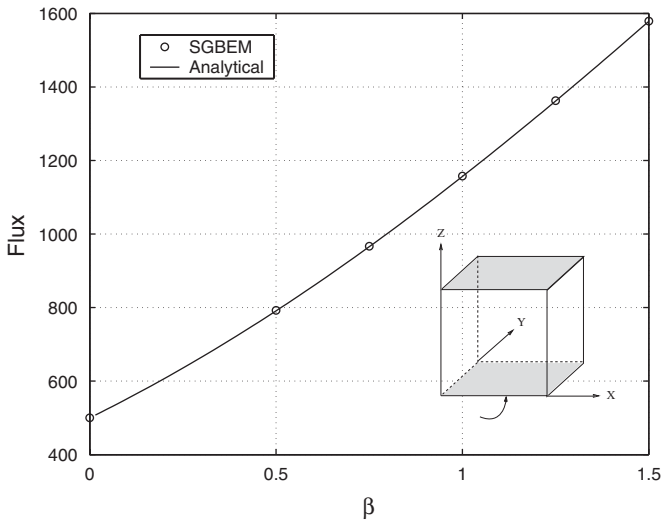

Figure 12. Variation of flux on the face $z = 0$ for different values of the material non-homogeneity parameter β.

Table I. Global error ($\mathscr{E}$) estimates on the boundary for FGM cube ($\beta = 1.0$).

			Global error $\mathscr{E}$ estimates	
Mesh	No. of nodes	No. of elements	Potential	Flux
1	54	48	0.0155	0.0303
2	96	108	0.0091	0.0165
3	150	192	0.0063	0.0123
4	294	432	0.0041	0.0101

the variation of the thermal conductivity is in a direction 45° off the z-axis, as shown in Figure 13. With this change, the problem becomes more interesting than the previous example because the heat flux is no longer constant on the two faces. The thermal conductivity is

$$k(x, y, z') = k_0 e^{2\beta z'} = 5e^{1.5z'} \tag{79}$$

where z' is an axis 45° off the z-axis (see Figure 13). The SGBEM solution is compared with an FEM solution obtained from a commercial package ABAQUS [35] using 20 node quadratic brick elements. In the FEM simulation, 10 homogeneous layers (see Figure 14) were used to approximate the continuous grading and the conductivity of each layer was computed using Equation (79), where z' was taken as the z'-co-ordinate of the layer centroid. It should be mentioned that FEM is not restricted to using the discontinuous piece-wise constant approximation available in existing commercial packages. It is possible to incorporate continuous grading within individual elements, and codes with this capability have been developed [15, 36],

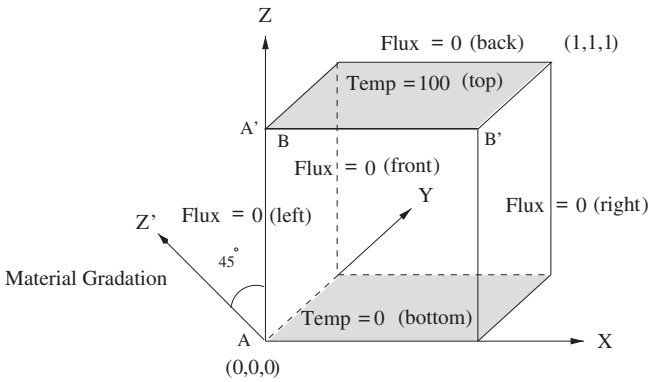

Figure 13. Geometry and boundary conditions of the FGM cube problem with material gradation in 45° with the z-axis. The faces with prescribed temperature are shaded.

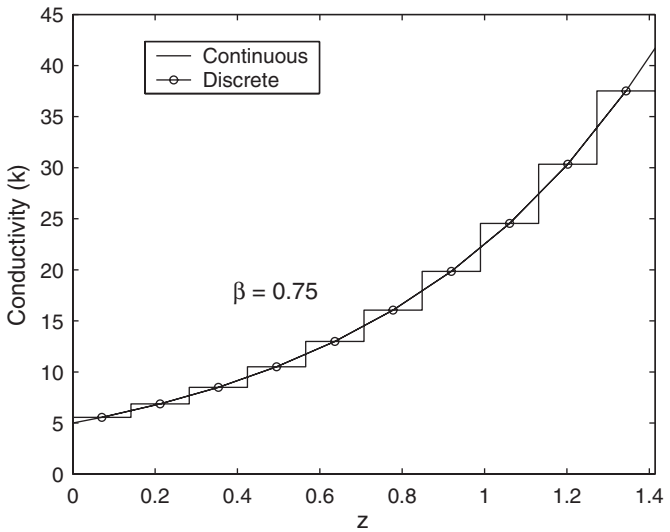

Figure 14. Continuous (used in BEM) and discrete (used in the FEM) representation of the conductivity k considering $\beta = 0.75$.

including a 3D public domain code WARP3D [37, 38]. The FEM mesh for the problem, shown in Figure 13, consists of 4961 nodes and 1000 elements. The temperature distribution along AA' in the $Y = 0$ plane (see Figure 13) with different values of β is plotted against the corresponding FEM solution in Figure 15. Also the flux distribution at the edge of the top face (along BB') is plotted with different values of β and compared with the FEM solution in Figure 16. Both of the SGBEM solutions agree with the FEM results within plotting accuracy.

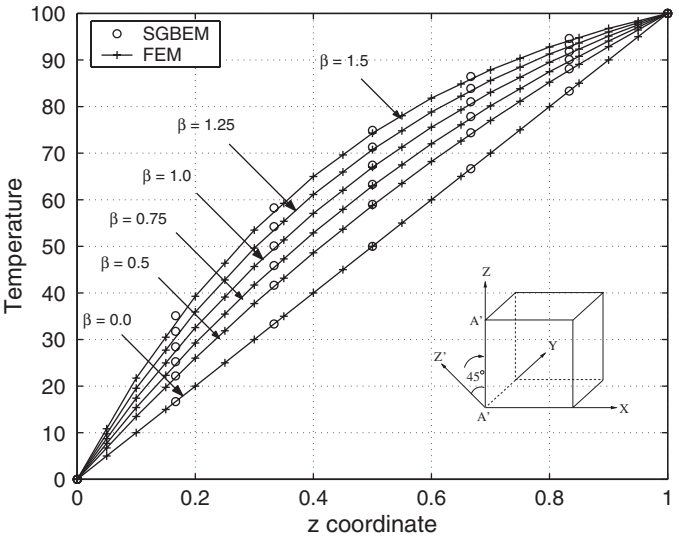

Figure 15. Temperature profile along edge AA' (in z direction) for the FGM cube problem.

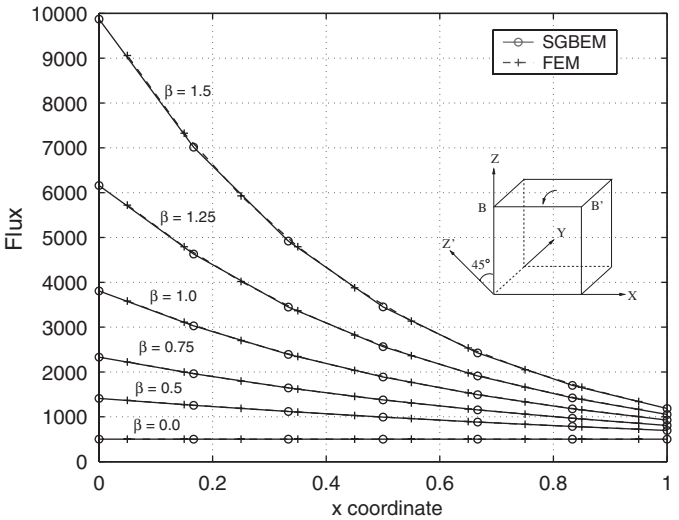

Figure 16. Flux distribution along BB' (in x direction) for the FGM cube problem.

5.3. Interior Neumann FGM-sphere problem

This example is an interior Neumann problem with prescribed boundary flux on the surface of the unit FGM sphere illustrated by Figure 17. The thermal conductivity is defined as

$$k(x, y, z) = k_0 e^{2\beta z} = 5e^{2\beta z} \tag{80}$$

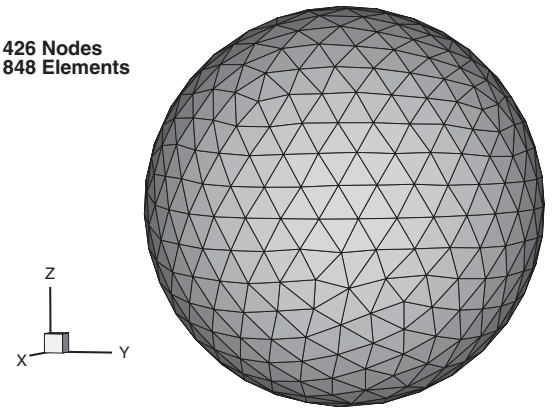

Figure 17. The mesh of the FGM unit sphere graded along the z direction.

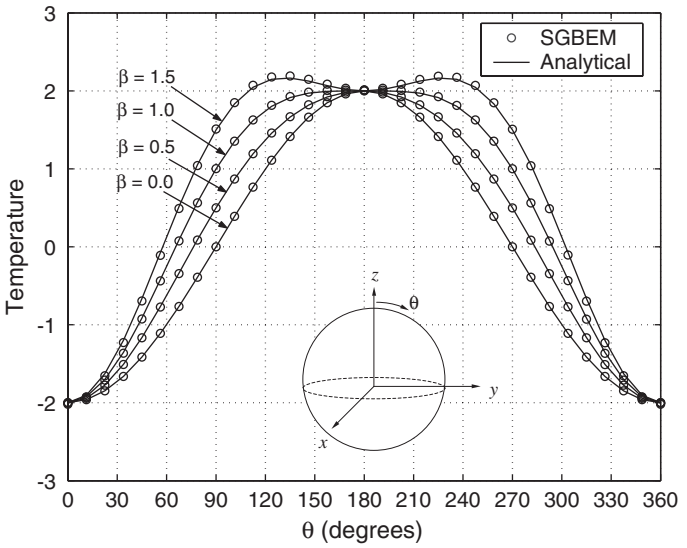

Figure 18. Temperature variation with θ (degrees) in $X = 0$ plane.

and the prescribed flux is

$$q(x, y, z) = -2k_0 e^{2\beta z}(\beta(x^2 + y^2) - z) \tag{81}$$

The exact solution for the surface temperature is

$$\phi(x, y, z) = \beta(x^2 + y^2) - 2z \tag{82}$$

As this is an interior Neumann problem, the solution is not unique, and an arbitrary constant can be added to the temperature. To enforce a unique solution, the temperature at $(x, y, z) = (0, 0, 1)$ was specified to be the value given by the analytical solution. The sphere is discretized

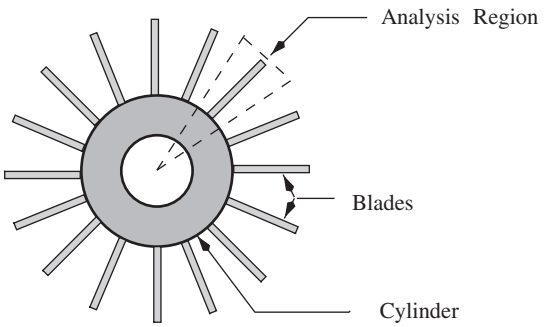

Figure 19. Top view of the compressor.

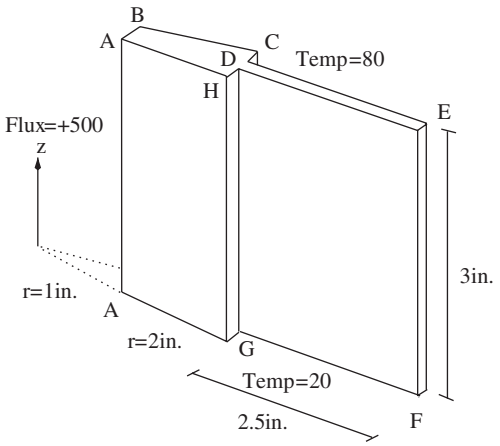

Figure 20. The geometry and the boundary conditions of the analysis region.

using 426 nodes and 848 elements (see Figure 17). The accuracy of the results obtained serve to verify the hypersingular BIE formulation as this equation is employed for the Neumann problem. It is also a good check if the limit to the boundary is correctly picking up on the surface orientation. The surface temperature is plotted against θ along the boundary where the $X = 0$ plane intersects the sphere and compared with analytical solution in Figure 18 for different values of β. The symmetry of the solution is captured by the SGBEM (cf. temperature variation from 0 to 180° and from 180 to 360°). Moreover, the numerical results agree with the analytical ones within plotting accuracy.

5.4. FGM compressor blade

A 3D analysis is performed on a one stage compressor where blades are attached to the main rotating components as shown in Figure 19. The transient response of a rotor made of homogeneous material with similar geometry has been investigated by Benz and Rencis [39] by coupling 2D and axisymmetric boundary zones. The compressor consists of a cylinder with 24 equally spaced blades attached to it. A 15° segment is used for the 3D analysis due to

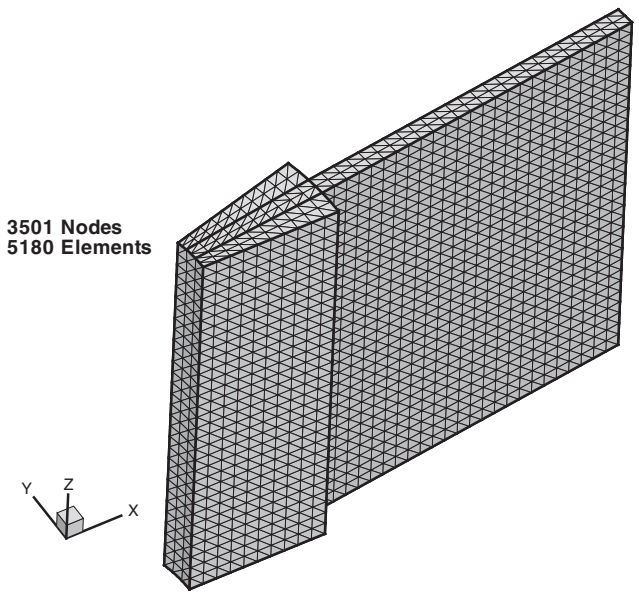

Figure 21. The boundary element mesh for the analysis region of the compressor.

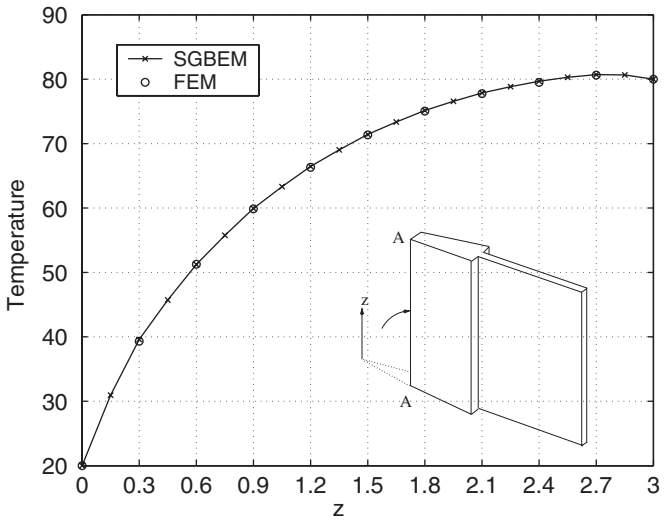

Figure 22. Temperature distribution in z direction at edge of the blade.

symmetry. The grading direction is the z-axis and the thermal conductivity varies according to

$$k(z) = 20\mathrm{e}^{0.46z} \tag{83}$$

The geometry, boundary condition and the BEM mesh are shown in Figures 20 and 21.

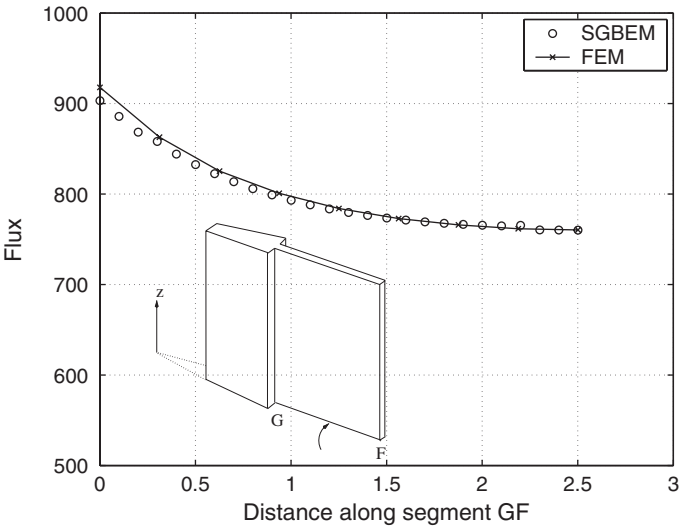

Figure 23. Flux distribution along segment GF of the blade.

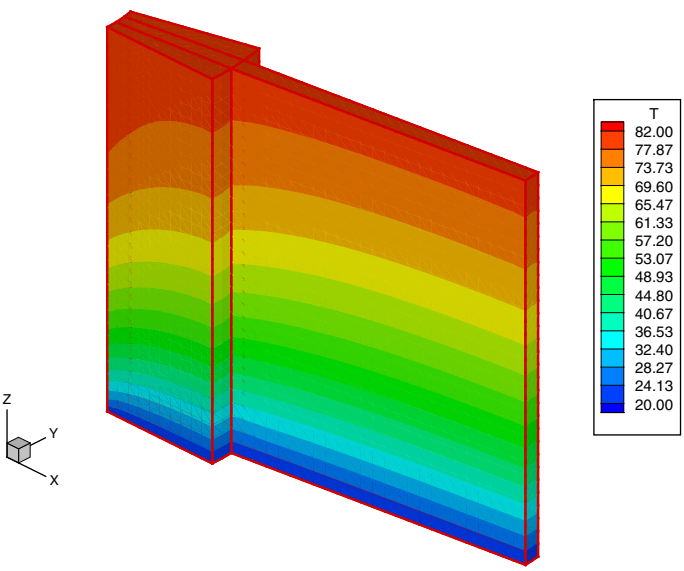

Figure 24. BEM contour plot of the temperature of the blade.

The BEM mesh consists of 5180 linear elements and 3501 nodes. The BEM solution is compared with an FEM solution obtained from the commercial package ABAQUS [35] using 20 node quadratic brick elements. In the FEM simulation 10 homogeneous layers were used to approximate the continuous grading, the conductivity of each layer was computed using Equation (83), where z was taken as the z-co-ordinate of the layers centroid (see previous

section for comments about FEM modelling of FGMs). The FEM mesh employed 903 nodes and 130 elements. The temperature distribution along the corner edge (which includes Point A) is plotted in Figure 22. The flux distribution along edge GF is plotted in Figure 23 and compared with the corresponding FEM solution. The minimal discrepancy can be attributed to the relatively coarse mesh of the FEM solution. Finally a contour plot of the temperature distribution is shown in Figure 24.

6. CONCLUSIONS

Symmetric Galerkin boundary element analysis, and the direct 'limit to the boundary' approach for evaluation of the hypersingular and singular integrals, can be successfully applied to FGMs. For exponentially graded (non-homogeneous) materials, the FGM Green's function can be determined and a boundary-only formulation can be obtained. The numerical results presented in this paper indicate that it is quite feasible to implement the complicated FGM Green's function (and its derivatives) in a standard boundary integral (symmetric Galerkin) approximation, and that accurate results are obtained. In particular, the present SGBEM for FGMs can also handle crack geometries [4] as the hypersingular equation has been successfully implemented.

APPENDIX A

The following codes were implemented with Maple 7.0. Only a few basic Maple operations, integration and substitution, are employed, and thus it is likely that, with relatively minor changes, these scripts would work with other symbolic computation systems. The code shows the analytical integration to extract the divergent terms for the coincident case and the edge adjacent case. The naming of variables follows the notation in this paper fairly closely, and it is therefore hoped that the codes are mostly self-explanatory. For convenience, references to the equations in the paper corresponding to the code are provided. However a few comment lines, which begin with the pound sign(#), are also included.

A.1. Analytical integration for coincident case

```
# This Maple file shows the analytical integration to extract
  divergent terms
# for the coincident case.

#  Ref: A. Sutradhar, G. H. Paulino, L. J. Gray
# "On hypersingular surface integrals in the symmetric Galerkin
  boundary
#  element method: Application to heat conduction in exponentially
  graded materials"
#  International Journal for Numerical Methods in Engineering

> restart;
> with(linalg):
```



```
> with(codegen,fortran);

# Initialize arrays
> phi:=array(0..2,0..1);
> Lterm:=array(0..3,0..1);
> phi_h:=array(0..3,0..1);
> jnp:=array(0..3);

# P -->  P+ eps N
# Equation (30)
> rh:=(eps^2+a^2*rho^2)^(1/2);
> jnr:=-eps*jp;

# Kernels
> ker:=3*jnr^2/rh^5-jp^2/rh^3+3*b00*jnr^2/rh^4+b00^2*jnr^2/rh^3
       -b00*jp^2/rh^2-b00^2*jnp[3]^2/rh;
# Equation (26)


# Taylor expansion
> expo1:=b00*(-rh+alpha*rho);
> exp1:=1+expo1;
# Equation (36)

# integrand
> ker:=ker*exp1;

# Loop for m=0 and m=1
> for j from 0 to 1 do

# first analytical integration
> zz:=int(rho^(j+1)*ker,rho=0..QR);
# Equation (37)

# Simplification
> zz:=expand(zz);
> zz := subs((eps^2)^(5/2)=eps^5,1/(eps^2)^(5/2)=1/eps^5,
sqrt(a^2)=a,1/sqrt(a^2)=1/a,sqrt(eps^2)=eps,1/sqrt(eps^2)
=1/eps,zz);
> zz:=expand(zz);
> zz:= subs(ln(eps^2)=2*loge,zz);

# loge term which are not the real divergent term
> zz:= collect(zz,loge);
> zz_log_koef:=coeff(zz,loge,1);
> zz_log_koef:=simplify(zz_log_koef);
```



```
> zz_log_koef:=simplify(subs(eps=0,zz_log_koef));
> zz:=coeff(zz,loge,0);

# second polar transformation
> zz  := subs(QR=Lambda,zz);
> zz  :=  zz*sp;
> zz  := expand(zz);
> zz  := normal(zz);
> zz:=expand(zz);
> zz:=simplify(zz);
> zz:=subs(ln(a*Lambda+sqrt(eps^2+a^2*Lambda^2))=ln(2*a*Lambda),
  zz);
> zz:=subs(arctan(a*Lambda/eps)=Pi/2,zz);
> zz:=subs(ln(eps^2+a^2*Lambda^2)=2*ln(a*Lambda),zz);
> zz:=expand(zz);

# Second Taylor expansion
> expo2:=b00*(2*zz2*Lambda);
> exp2:=1+expo2+expo2^2/2;
# Equation (51)
> zz:=zz*exp2;

# Second analytical integration
# Loop for s=0,1,2


> for k from 0 to 2 do
> phi[k,j]:= int(Lambda^k*zz,Lambda=0..QL);
# Equation (52)
> phi[k,j]:= subs((eps^2)^(5/2)=eps^5,1/(eps^2)^(5/2)=1/eps^5,
          (eps^2)^(3/2)=eps^3,1/(eps^2)^(3/2)=1/eps^3,sqrt(a^2)=a,
    1/sqrt(a^2)=1/a, sqrt(eps^2)=eps,1/sqrt(eps^2)=1/eps,phi[k,j]);
> phi[k,j]:=subs(sqrt(eps^2+a^2*QL^2)=a*QL,1/sqrt(eps^2+a^2*QL^2)
           =1/(a*QL),phi[k,j]);
> phi[k,j]:=subs(arctan( a*QL/eps)=pi/2,phi[k,j]);
> phi[k,j]:= subs(ln((eps^2+a^2*QL^2)/eps^2)=ln(eps^2+a^2*QL^2)
           -ln(eps^2),phi[k,j]);
> phi[k,j]:= subs(ln(eps^2)=2*loge,phi[k,j]);
> phi[k,j]:= expand(phi[k,j]);
> Lterm[k,j] := coeff(phi[k,j],loge);
> Lterm[k,j] := subs(eps=0,Lterm[k,j]);
# Equation (55)
> phi[k,j]   := coeff(phi[k,j],loge,0);
> phi[k,j]   := collect(phi[k,j],eps);

# set eps ---> 0
```



```
> phi[k,j]  := subs(eps=0,phi[k,j]);
> phi[k,j]  := normal(expand(phi[k,j]));
> phi[k,j]:=subs(ln(a^2*QL^2)=2*ln(a*QL),1/(a^2*QL^2)^(3/2)
        =1/(a^3*QL^3),
(a^2*QL^2)^(3/2)=(a^3*QL^3),phi[k,j]);
> phi[k,j]  := expand(phi[k,j]);

# check with Laplace equation for homogenous material
# b00:=0;
> phi_h[k,j]  := simplify(subs(b00=0,phi[k,j]));
> Lterm[k,j] ;
> od;
> od;

# print results
# m=0
> for k from 0 to 2 do
> phi[k,0];
> phi_h[k,0];
> Lterm[k,0];
> od;

# m=1
> for k from 0 to 2 do
> phi[k,1];
> phi_h[k,1];
> Lterm[k,1];
> od;

# Convert to Fortran
> fortran(phi);
> fortran(Lterm);
```

A.2. Analytical integration for edge adjacent case

```
# This Maple file shows the analytical integration to extract
  divergent terms
# for the edge adjacent case.

#  Ref: A. Sutradhar, G. H. Paulino, L. J. Gray
# "On hypersingular surface integrals in the symmetric Galerkin
  boundary
#  element method: Application to heat conduction in exponentially
  graded materials"
#  International Journal for Numerical Methods in Engineering
```



```
> restart;
> with(linalg):
> with(codegen,fortran):

# Initialize arrays
> jnp:=array(1..3);
> jnq:=array(1..3);
> phi  := array(0..2);
> sng  := array(0..2);

# P -->  P+ eps N
> rh  := (eps^2 + eps*a1*Lambda + a2*Lambda^2)^(1/2);
# Equation (65)
> ##
> ## kernel
> ##  Note: cos(psi) factor from jacobian product omitted
> ##
> jNR:=(j1p*Lambda-jnpL*eps);
> jnR:=j1q*Lambda-jnqL*eps;
> nz:=jnq[3];
> Nz:=jnp[3];

# Kernels
# Equation (26)
> hyp:=3*jnR*jNR/rh^5+3*b00*jnR*jNR/rh^4+(b00^2*jnR*jNR-b00*
      (Nz*jnR-nz*jNR) -ndN)/rh^3-b00*((b00*(Nz*jnR-nz*jNR)
       +ndN)/rh^2)-b00^2*Nz*nz/rh;
> hyp:=Lambda^2*hyp;

# Taylor expansion
> exp_term:=1;
# Equation (67)

# integrand
> exp_hyp:=exp_term*hyp;

# Loop for s=0,1,2
> ## powers from shape function product
> for ll from 0 to 2 do
> phi[ll]:= Lambda^ll*exp_hyp;

# Analytical integration
> phi[ll] := int(phi[ll],Lambda=0..QL);
# Equation (63)

# Simplification
```



```
> phi[ll] := subs((eps^2)^(5/2)=eps^5,
  ln((eps*a1+2*eps*sqrt(a2))/a2^(1/2))
  =loge+ln(a1/a2^(1/2)+2),
> sqrt(eps^2*a1^2-4*a2*eps^2)=eps*sqrt(a1^2-4*a2),ln(eps^2)
  =2*loge,
> arctanh(eps*a1/(eps^2*a1^2-4*a2*eps^2)^(1/2))
  =arctanh(a1/(a1^2-4*a2)^(1/2)),
> arctanh((2*a2*QL+eps*a1)/(eps^2*a1^2-4*a2*eps^2)^(1/2))
  =1/2*ln(2*a2*QL)-1/2*ln(-2*a2*QL),
> 1/(eps^2)^(5/2)=1/eps^5,1/sqrt(eps^2*a1^2-4*a2*eps^2)
  =1/(eps*sqrt(a1^2-4*a2))
,ln((eps*a1+2*sqrt(eps^2)*sqrt(a2))/a2^(1/2))
  = loge+ln(a1/a2^(1/2)+2),
(eps^2)^(3/2)=eps^3,1/(eps^2)^(3/2)=1/eps^3
> ,phi[ll]);
> phi[ll] := expand(phi[ll]);

# set eps ---> 0
> phi[ll] := subs(eps=0,phi[ll]);
> sng[ll] := normal(coeff(phi[ll],loge,1));
# Equation (68)
> phi[ll] := normal(coeff(phi[ll],loge,0));
> phi[ll]:=expand(phi[ll]);
> phi[ll]:=simplify(phi[ll]);
> end do;
# Convert to Fortran
> fortran(phi);
```


ACKNOWLEDGEMENTS

We acknowledge the support from the Computational Science and Engineering (CSE) Program (Prof. Michael Heath, Director) at the University of Illinois at Urbana-Champaign (UIUC) for the CSE Fellowship award to A. Sutradhar. G. H. Paulino acknowledges the support from the National Science Foundation under Grant CMS-0115954 (Mechanics and Materials Program). Work at Oak Ridge National Laboratory (ORNL) was supported by the Applied Mathematical Sciences Research Program of the Office of Mathematical, Information, and Computational Sciences, U.S. Department of Energy under Contract DE-AC05-00OR22725 with UT-Battelle, LLC.

REFERENCES

1. Hartmann F, Katz C, Protopsaltis B. Boundary elements and symmetry. *Ingenieur-Archiv* 1985; **55**:440–449.
2. Hölzer SM. The symmetric Galerkin BEM for plane elasticity: scope and applications. In *Numerical Methods in Engineering 92*, Hirsch C (ed.). Elsevier: Amsterdam, 1992.
3. Sirtori S, Maier G, Novati G, Miccoli S. A Galerkin symmetric boundary element method in elasticity: formulation and implementation. *International Journal for Numerical Methods in Engineering* 1992; **35**: 255–282.
4. Bonnet M, Maier G, Polizzotto C. Symmetric Galerkin boundary element method. *Applied Mechanics Reviews* (ASME) 1998; **51**:669–704.

5. Paulino GH, Gray LJ. Galerkin residuals for error estimation and adaptivity in the symmetric Galerkin boundary integral method. *Journal of Engineering Mechanics* (ASCE) 1999; **125**(5):575–585.
6. Carini A, Diligenti M, Maranesi P, Zanella M. Analytical integrations for two dimensional elastic analysis by the symmetric Galerkin boundary element method. *Computational Mechanics* 1999; **23**:308–323.
7. Frangi A, Novati G. Symmetric BE method in two-dimensional elasticity: evaluation of double integrals for curved elements. *Computational Mechanics* 1996; **19**:58–68.
8. Hölzer SM. How to deal with hypersingular integrals in the symmetric BEM. *Communications in Numerical Methods in Engineering* 1993; **9**:219–232.
9. Salvadori A. Analytical integrations in 2D BEM elasticity. *International Journal for Numerical Methods in Engineering* 2002; **53**:1695–1719.
10. Li S, Mear ME, Xiao L. Symmetric weak form integral equation method for three-dimensional fracture analysis. *Computer Methods in Applied Mechanics and Engineering* 1998; **151**:435–459.
11. Frangi A, Novati G, Springhetti R, Rovizzi M. 3D fracture analysis by the symmetric Galerkin BEM. *Computational Mechanics* 2002; **28**:220–232.
12. Frangi A. Fracture propagation in 3D by the symmetric Galerkin boundary element method. *International Journal of Fracture* 2002; **116**:313–330.
13. Kuhn G, Haas M. A symmetric Galerkin BEM implementation for 3D elastostatic problems with an extension to curved elements. *Computational Mechanics* 2002; **28**:250–259.
14. Miyamoto Y, Kaysser WA, Rabin BH, Kawasaki A, Ford RG. *Functionally Graded Materials: Design, Processing and Applications*. Kluwer Academic Publishers: Dordrecht, 1999.
15. Paulino GH, Jin ZH, Dodds RH Jr. Failure of functionally graded materials. In *Comprehensive Structural Integrity*, Karihaloo B, Knauss WG (eds), vol. 2. Chapter 13. Elsevier Science: Amsterdam, 2003; 607–644.
16. Gray LJ, Kaplan T, Richardson JD, Paulino GH. Green's functions and boundary integral analysis for exponentially graded materials: heat conduction. *Journal of Applied Mechanics* (ASME) 2003; **70**:543–549.
17. Sutradhar A, Paulino GH, Gray LJ. Transient heat conduction in homogeneous and nonhomogeneous materials by the Laplace transform Galerkin boundary element method. *Engineering Analysis with Boundary Elements* 2002; **26**:119–132.
18. Sutradhar A, Paulino GH, Gray LJ. Erratum to Transient heat conduction in homogeneous and non-homogeneous materials by the Laplace transform Galerkin boundary element method. *Engineering Analysis with Boundary Elements* 2003; **27**:639.
19. Tanaka M, Matsumoto T, Suda Y. A dual reciprocity boundary element method applied to the steady-state heat conduction problem of functionally gradient materials. *Electronic Journal of Boundary Elements* 2002; **1**:128–135.
20. Cheng AHD. Darcy's flow with variable permeability: a boundary integral solution. *Water Resources Research* 1984; **20**:980–984.
21. Cheng AHD. Heterogeneities in flows through porous media by the boundary element method. In *Topics in Boundary Element Research*, Brebbia CA (ed.), vol. 4. Applications in geomechanics, Chapter 6. Springer: Berlin, 1987; 129–144.
22. Ervin VJ, Stephan EP. A boundary element Galerkin method for a hypersingular integral equation on open surfaces. *Mathematical Methods in the Applied Sciences* 1990; **13**:281–289.
23. Frangi A. Regularization of boundary element formulations by the derivative transfer method. In *Singular Integrals in Boundary Element Methods*, Sladek V, Sladek J (eds). Advances in boundary elements, Chapter 4. Computational Mechanics Publishers: Southampton, 1998; 125–164.
24. Hadamard J. *Lectures on Cauchy's Problem in Linear Partial Differential Equations*. Dover Publications: New York, 1952.
25. Aimi A, Diligenti M. Hypersingular kernel integration in 3D Galerkin boundary element method. *Journal of Computational and Applied Mathematics* 2002; **138**:51–72.
26. Carini A, Salvadori A. Analytical integrations 3D BEM. *Computational Mechanics* 2002; **28**:177–185.
27. Salvadori A. Analytical integrations of hypersingular kernel in 3D BEM problems. *Computer Methods in Applied Mechanics and Engineering* 2001; **190**:3957–3975.
28. Gray LJ, Kaplan T. 3D Galerkin integration without Stokes' theorem. *Engineering Analysis with Boundary Elements* 2001; **25**:289–295.
29. Gray LJ, Glaeser J, Kaplan T. Direct evaluation of hypersingular Galerkin surface integrals. *SIAM Journal on Scientific Computing* 2004; **25**:1534–1556.
30. Li BQ, Evans JW. Boundary element solution of heat convection–diffusion problems. *Journal of Computational Physics* 1991; **93**:255–272.

31. Paulino GH, Sutradhar A, Gray LJ. Boundary element methods for functionally graded materials. In *Boundary Element Technology*, Brebbia CA, Dippery RE (eds), vol. XV, Section 3. WIT Press: Southampton, 2003; 137–146.
32. Bonnet M. *Boundary Integral Equation Methods for Solids and Fluids*. Wiley: England, 1995.
33. Lutz ED, Gray LJ. Exact evaluation of singular boundary integrals without CPV. *Communications in Numerical Methods in Engineering* 1993; **9**:909–915.
34. Gray LJ, Paulino GH. Crack tip interpolation, revisited. *SIAM Journal of Applied Mathematics* 1998; **58**: 428–455.
35. *ABAQUS Version 6.2*. Hibbitt, Karlsson and Sorensen, Inc.: Pawtucket, RI, USA, 2002.
36. Kim JH, Paulino GH. Isoparametric graded finite elements for nonhomogeneous isotropic and orthotropic materials. *Journal of Applied Mechanics* (ASME) 2002; **69**:502–514.
37. Walters MC, Paulino GH, Dodds RH Jr. Stress intensity factors for surface cracks in functionally graded materials under mode I thermomechanical loading. *International Journal of Solids and Structures* 2004; **41**:1081–1118.
38. Gullerud AS, Koppenhoefer KC, Roy A, Dodds RH. WARP3D-Release 13.18 Manual. *Technical Report UILU-ENG-95-2012*, Civil Engineering, University of Illinois at Urbana-Champaign, Urbana, IL, 2000.
39. Benz UA, Rencis JJ. Coupling two-dimensional and axisymmetric boundary element zones for transient heat transfer applications. *Engineering Analysis with Boundary Elements* 2002; **26**:455–467.

